Unusual band renormalization in the simplest iron-based superconductor FeSe$_{1-x}$

J. Maletz,[1] V. B. Zabolotnyy,[1] D. V. Evtushinsky,[1] S. Thirupathaiah,[1] A. U. B. Wolter,[1] L. Harnagea,[1] A. N.Yaresko,[2]
A. N. Vasiliev,[3,4] D. A. Chareev,[5,6] A. E. Böhmer,[7] F. Hardy,[7] T. Wolf,[7] C. Meingast,[7] E. D. L. Rienks,[8]
B. Büchner,[1,9] and S. V. Borisenko[1]

[1]*Institute for Solid State Research, IFW Dresden, P.O. Box 270116, D-01171 Dresden, Germany*
[2]*Max Planck Institute for Solid State Research, Heisenbergstrasse 1, D-70569 Stuttgart, Germany*
[3]*Low Temperature Physics and Superconductivity Department, Physics Faculty, Moscow State University, Moscow 119991, Russia*
[4]*Theoretical Physics and Applied Mathematics Department, Institute of Physics and Technology,*
Ural Federal University, 620002 Ekaterinburg, Russia
[5]*National Research University Higher School of Economics, 20 Myasnitskaya Ulitsa, Moscow 101000, Russia*
[6]*Institute of Experimental Mineralogy, Russian Academy of Sciences, Chernogolovka, Moscow Region 142432, Russia*
[7]*Institute für Festkörperphysik, Karlsruhe Institute für Technologie, 76021 Karlsruhe, Germany*
[8]*Helmholtz-Zentrum Berlin, Albert-Einstein-Strasse 15, 12489 Berlin, Germany*
[9]*Institut für Festkörperphysik, Technische Universität Dresden, D-01171 Dresden, Germany*
(Received 5 June 2013; revised manuscript received 2 June 2014; published 18 June 2014)

The electronic structure of the iron chalcogenide superconductor FeSe$_{1-x}$ was investigated by high-resolution angle-resolved photoemission spectroscopy (ARPES). The results were compared to DFT calculations showing some significant differences between the experimental electronic structure of FeSe$_{1-x}$, DFT calculations, and existing data on FeSe$_x$Te$_{1-x}$. The bands undergo a pronounced orbital-dependent renormalization, different from what was observed for FeSe$_x$Te$_{1-x}$ and any other pnictides.

It is well established that the iron arsenic/selenium layers, common for all the recently found and investigated iron-based superconductors, are responsible for the superconductivity in these compounds [1]. The binary "11" family of FeSe$_{1-x}$ and FeSe$_x$Te$_{1-x}$ offers the possibility to investigate systems consisting of just these layers without the intermediate layers which are present in the "111," "122," and "1111" families. This simplest iron-based superconductor may therefore yield valuable information about the origin of superconductivity in the iron pnictides/chalcogenides. The FeSe$_x$Te$_{1-x}$ "11" system exhibits long-range antiferromagnetic (AFM) order for its end member FeTe which is suppressed for $x > 0.1$, whereas a short-range antiferromagnetic order appears for the intermediate range $0.1 < x < 0.45$ [2,3]. Superconductivity is observed for $x > 0.2$ to 0.45 [3,4], thus coexisting with the AFM also for the highest T_c composition of FeSe$_{0.4}$Te$_{0.6}$ [4]. The end member FeSe has a T_c of $\sim$8 K [5]. Recently, in a study on single-layer FeSe grown on a SrTiO$_3$ substrate, superconductivity with a T_c of up to 55 K [6] was reported. Further studies on this system found an onset of superconductivity at up to 65 K [7]. There are also several angle-resolved photoemission spectroscopy (ARPES) studies on FeSe$_x$Te$_{1-x}$ compounds, yielding interesting and in part contradicting results. Depending on x, the position of the bands at the $\overline{\Gamma}$ point with respect to E_F may vary. For $x = 0.34$, all three low-energy bands are crossing the Fermi level [8]; for $x = 0.3$ to 0.45 only two of them are crossing E_F [9–12]. For the monolayer FeSe, no Fermi surface in the zone center was observed at all [13]. Additionally, there are diverging interpretations concerning the renormalization of the bands, both in size and orbital character of the affected bands. There is no general agreement on the electronic structure of these compounds and whether a comparison between the Te-substituted samples and the FeSe monolayers is valid. This issue can be addressed

by investigating FeSe$_{1-x}$ single crystals, as this allows for more precise quantitative statements about the deviations from the DFT on FeSe calculations and provides valid data for comparison with the FeSe monolayers.

Here we report on ARPES studies of FeSe$_{0.96}$ and FeSe$_{1.00}$ single crystals. The different samples were grown using the KCl/AlCl$_3$ flux method and the low-temperature vapor-transport technique, characterized with x-ray diffraction and EDX and investigated by low-temperature specific heat measurements and high-resolution thermal-expansion measurements showing a T_c of 7.7 K to 9 K [14–16]. ARPES measurements were performed at the BESSY2 synchrotron facility. Samples were mounted on the cryomanipulator of the 1^3-ARPES station and cleaved at a temperature of $T \sim 40$ K in ultrahigh vacuum with a base pressure of $\sim$10^{-11} mbar. Spectra were taken using excitation energies ranging from 20 eV to 120 eV and temperatures down to 890 mK. The overall energy and angular resolutions were $\Delta E = 4$ meV and $\Delta \eta = 0.2°$, respectively. DFT calculations were performed for the experimental crystal structure of FeSe from Ref. [17] with $z_{Se} = 0.2672$, yielding good agreement with the results of other calculations [18] but differring from calculations using the optimized crystal structure [19].

Figures 1(a) and 1(b) show intensity maps of the k_x-k_y planes at the Fermi energy (E_F) and at $E_{bind} = 35$ meV measured by ARPES. These spectra were taken at an excitation energy of $h\nu = 80$ eV and integrated over an energy interval of ± 5 meV. Panel (c) shows the Fermi surface contours from DFT calculations. The maps exhibit two features, a circular hole-like Fermi surface around the $\overline{\Gamma}$ point (the feature's diameter grows with increasing binding energy) and a small electron-like Fermi surface around the $\overline{M}$ point, which vanishes for higher binding energies and is replaced by a propeller-shaped feature originating from two hole-like bands
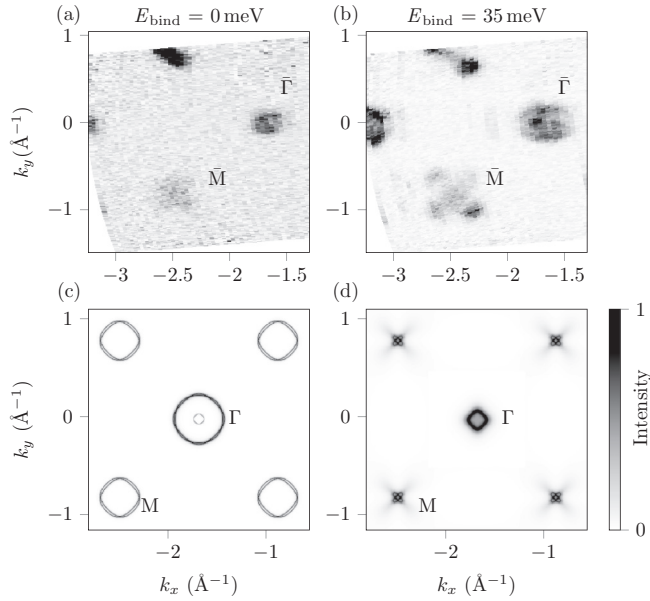
FIG. 1. k_x-k_y intensity map taken at (a) E_F and at (b) $E_{bind} = 35$ meV as measured by ARPES at $T = 40$ K with photon energy $h\nu = 80$ eV and linear horizontal (LH) polarization. Spectra were energy integrated over an interval of ± 5 meV and thus include spectral weight from higher and lower binding energies. (c) Fermi surface from DFT calculations. (d) Calculated Fermi surface including band renormalizations and shifts, energy integrated over an interval of ± 5 meV.

closing just beneath E_F at the $\overline{M}$ point. Comparing spectra and contours predicted by DFT, differences in both size and number of the Fermi surface sheets can be found. While from the calculations three Fermi surface sheets are expected around the Γ point, the ARPES spectra show that there is only one. The Fermi momentum (k_F) of the Γ-hole-pocket obtained from ARPES is 0.05 Å^{-1} while calculations predict a k_F between 0.25 Å^{-1} and 0.3 Å^{-1}, which is 5 to 6 times larger than measured. The situation for the electron pockets located around the M points of the Brillouin zone is similar. Here, the measured diameter is 0.18 Å^{-1} while the calculated diameter was found to be 0.37 Å^{-1}. Figure 2 allows for a closer look on the electronic structure at the Z point of the Brillouin zone (compare Fig. 4 for k_z location). Panels (a) and (b) contain energy-momentum cuts in the Z-R direction taken with a photon energy $h\nu = 25$ eV and two different polarizations. Panel (a) shows the cut corresponding to the linear horizontal (LH) polarization. Three bands can be identified. One of those, called α from hereon, crosses E_F to create a hole-like Fermi surface. From fitting the dispersion close to the Fermi energy, the top of this band is estimated to be at $E_{bind} = -3$ meV. A second hole-like band, called β, also approaches E_F, though closing at $E_{bind} = 15$ meV, and thus not forming a Fermi surface. A third, flatter band, called γ, can be identified at higher binding energies, strongly losing intensity towards lower binding energies. From fitting the branches at higher binding energies, the top of this band is estimated to be at $E_{bind} = 52$ meV. The fitted dispersions can also be seen in panel (b) which shows the same energy-momentum cut measured with linear vertical (LV) polarized light. In this
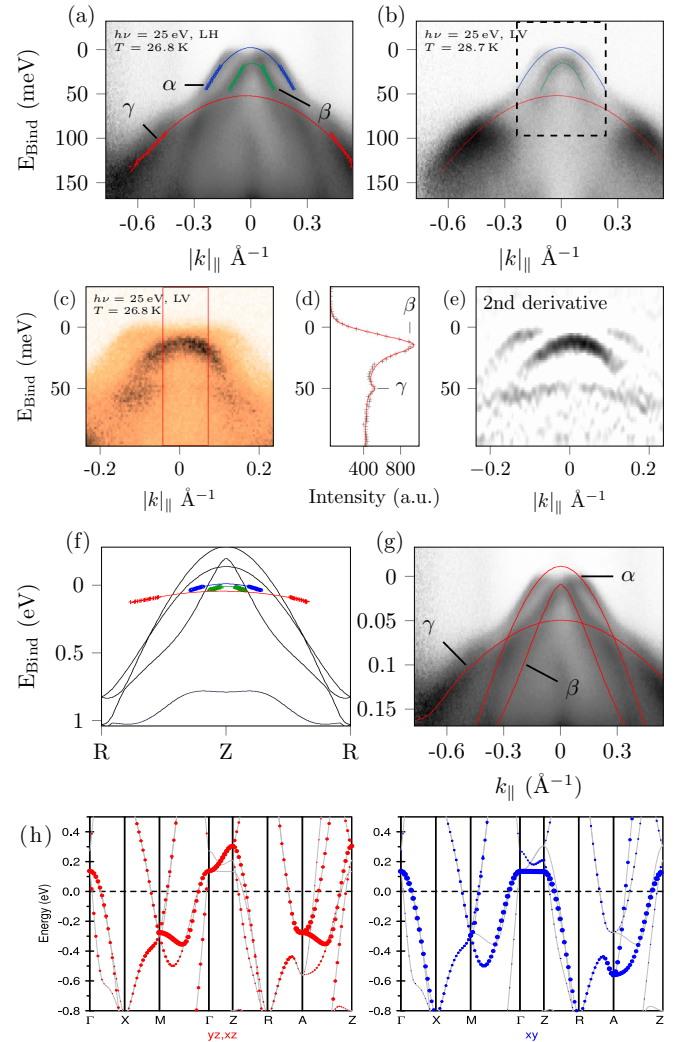
FIG. 2. (Color online) (a) Energy momentum cut taken at 26.8 K in Z-R direction with $h\nu = 25$ eV and linear horizontal (LH) polarization. The markers are the band dispersions derived from momentum distribution curves. The solid lines represent the expected band positions from fitting the obtained band positions. (b) Energy momentum cut taken at 28.7 K in Z-R direction with $h\nu = 25$ eV and linear vertical (LV) polarization. (c) Zoomed region from the dashed area in panel (b). (d) Integrated energy distribution curve (EDC) from the boxed area in panel (c). The EDCs were integrated over the full width of the box (36 channels). The marked peaks correspond to the tops of the β and γ bands. (e) Second derivative of the spectrum shown in panel (c). (f) Comparison of calculated (solid black lines) and experimental (colored, with markers) dispersions. (g) Comparison of experiment and calculations with applied renormalizations and shifts as stated in the text. (h) LDA-LMTO calculations of FeSe, including orbital character.

polarization the top of the β band is more prominent and matches the previously derived dispersion very well. Also, the top of the γ band can be located in this polarization. A magnification of the region close to E_F is shown in panels (c)–(e). To improve visibility of the γ band, the integrated energy distribution curve (EDC) from the framed area in panel (c) is shown along with the second derivative of the spectrum. The EDC from the center of the Brillouin zone exhibits two
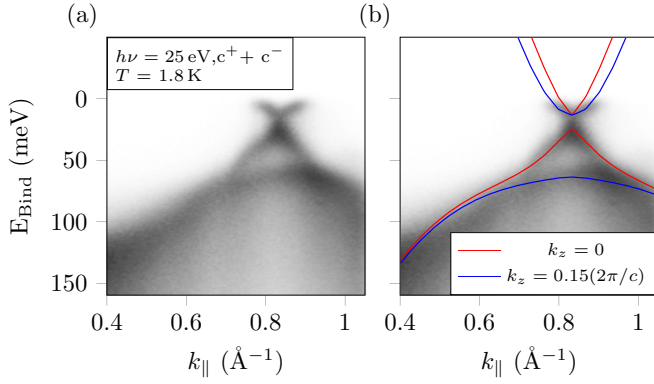
FIG. 3. (Color online) Photoemission spectra of the M point. (a) Sum of two spectra taken with $h\nu = 25$ eV in circular positive (c^+) and circular negative (c^-) polarization. (b) The same spectrum overlaid with calculations for two different k_z. The red lines mark the dispersion for $k_z = 0$; blue lines represent $k_z = 0.15(2\pi/c)$. Both calculations were adjusted using the same parameters; the difference is solely caused by the k_z shift.

peaks: one from the top of the β band at $E_{bind} = 15$ meV and the other one from the top of the γ band at $E_{bind} = 49$ meV, both in very good agreement with the positions estimated from the previous fits. All three bands can also be clearly identified in the second derivative plot in panel (e).

In Fig. 2(f), the experimental and the bare calculated dispersions are compared. It can be seen that the bands are renormalized. The α and β bands are renormalized by factors of ~ 3 and ~ 3.7, respectively, while the γ band is renormalized by a factor of ~ 9. This significantly differs from the previous studies on FeSe$_x$Te$_{1-x}$, where either a uniform renormalization of 2 [12,20] and 3.125 [8] had been observed, or a band-selective renormalization of 1, 6, and 17 [10] was reported, and is also unusual for iron-based superconductors in general. Additionally, band-dependent shifts have to be introduced to create a match between calculated and experimental band structure. The shifts are 0.09 eV, 0.065 eV, and 0.045 eV for the α, β, and γ bands, respectively. The shifted and renormalized calculation is compared with the experiment in Fig. 2(g) yielding excellent agreement (for further spectra see Supplemental Material [33]).

The band structure around the M points is presented in Fig. 3. Here, in panel (a), the sum of two spectra recorded with circular positive (c^+) and circular negative (c^-) polarization is shown. In the experimental data one can identify all the features predicted by the band structure calculations, namely, the shallow electron pockets and supporting hole-like dispersion. There are no additional bands or unusual splittings. The triangle of dispersions centered around (0.8 Å^{-1}, 50 meV) is created by a finite integration along k_z. We estimate this window as 0.15 $(2\pi/c)$. Panel (b) contains the same spectrum overlaid with calculations for $k_z = 0$ and $k_z = 0.15 (2\pi/c)$. These calculations were renormalized by a factor ~ 2 and shifted by 140 meV towards lower binding energies and follow the recorded spectral weight very well. The phenomenon that the calculated band structure has to be shifted in different directions for the center and corner of the Brillouin zone to match the experimental data has already been observed in ARPES

for other iron-pnictide compounds such as KFe$_2$As$_2$ [21] and LiFeAs [22], and in quantum oscillation experiments for LaFePO [23], and seems to be a common feature for these compounds. 1(d) shows the resulting Fermi surfaces when the shifts and renormalizations are applied to the DFT calculations, reproducing the experimental Fermi surface very well.

From the collected data, one can also determine the orbital character of the bands. This provides the possibility to find correlations between band renormalization and orbital character, which is important in light of the selective Mott transition, which recently received sentential attention, and where orbital-dependent behavior plays a major role [24,25]. Symmetry and geometry considerations (see Supplemental Material S4 [33]) lead to the conclusion that α and β bands consist of d_{xz}/d_{yz} orbitals. Therefore, the γ band has to be of d_{xy} character. This is supported by the fact that this band shows no k_z dispersion, as predicted for the d_{xy} band by calculations shown in Fig. 2(h).

Additional temperature and energy dependent measurements were performed at the Γ point. By using different excitation energies $h\nu$ in the range of 20 eV to 110 eV, measurements for different k_z along the Γ-Z direction were conducted. In Fig. 4(a) the evolution of the Γ Fermi surface sheet with excitation energy is shown. As seen before, only one α band crosses the Fermi level (for energy-momentum cuts and EDCs see Supplemental Material [33]). Agreement with the bare calculated dispersion [panel (c)] is not good. But if
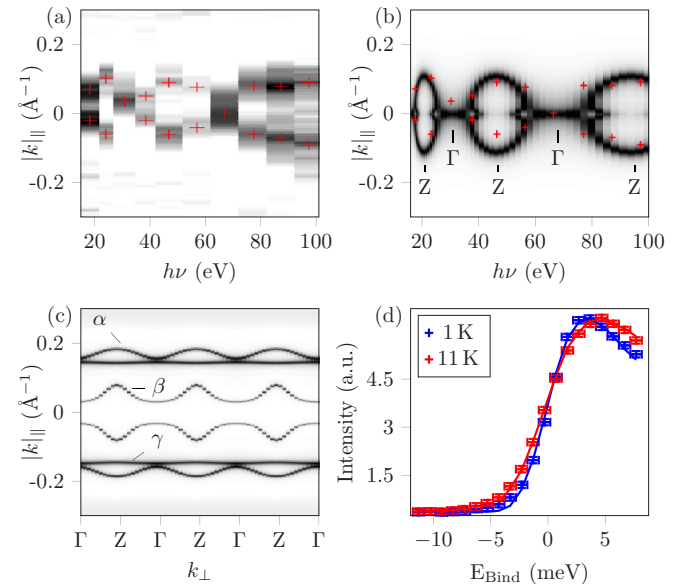
FIG. 4. (Color online) (a) Evolution of the $\overline{\Gamma}$ Fermi surface sheet with excitation energy. Markers indicate positions of maximum intensity. Energy momentum cuts and EDCs can be seen in the Supplemental Material [33]. (b) Calculated k_z dispersion in energy space. Calculation includes shifting and renormalization of the bands. Markers represent the experimental dispersion. (c) Bare calculation of the k_z dispersion in momentum space. (d) Energy distribution curves from Γ point at 1 K (superconducting state) and 11 K (normal state). Markers represent the experimental data; solid lines were obtained by fitting to modeled data.

the calculation is adjusted according to the previously derived band shifts and renormalizations, the agreement is excellent as can be seen in panel (b). The Γ point can now be identified with $h\nu \sim 30$ eV and $h\nu \sim 70$ eV, where the width of the feature is minimal, while the maximum width denotes the Z point. The α band thus creates a "cigar shaped" closed Fermi surface sheet around the Z point of the Brillouin zone. Similar features have been observed earlier and identified as a possible prerequisite for superconductivity in the iron pnictides [26].

To quantify the size of the superconducting gap, which is supposed to be in the range of 1.33 meV to 2.2 meV [14,27], we compared the experimental EDCs to EDCs obtained from modeled spectra [28] This comparison can be seen in Fig. 4(d). For 1 K (blue) and 11 K (red), the markers represent the experimental data while the solid lines show the EDCs from the modeled spectra. From fitting the model to the data, a maximum gap size of $\Delta_{\max} = 2$ meV with a BCS ratio of $2\Delta/k_B = 5.7$ is estimated, similar to the findings for $Fe_{1.03}Te_{0.7}Se_{0.3}$ [12], which suggests a strong coupling scenario.

We have thus shown that single-crystalline FeSe, the structurally simplest member of the iron-pnictide/iron-chalcogenide family, also exhibits the simplest Fermi surface consisting of only one closed "cigar shaped" hole pocket around the Z point of the Brillouin zone and a shallow, electron-like feature around the Brillouin zone corners (M point), probably consisting of two degenerate electron pockets. Due to the shallowness of the electron pockets it is hard to estimate the size of the corresponding Fermi surface sheets and thus to make a solid statement about the possibility of nesting. Temperature-dependent measurements yielded a maximum size of the superconducting gap of about 2 meV leading to a BCS ratio of 5.7. The d_{xz}/d_{yz} bands are renormalized by factors of 3 to 3.7, while the d_{xy} band is renormalized by a factor of 9. This strongly differs from the conclusions in the previously mentioned studies [8,10,12,20]. We do not find a uniform renormalization, but a strongly orbital-dependent one. But in contrast to Tamai *et al.* we find comparable renormalization for the d_{xz}/d_{yz}, while the d_{xy} shows a three times larger renormalization.

This orbital-dependent behavior can be explained in the picture of Hund metals and kinetic frustration [29]. Here, the mass enhancement of the $t2g$ orbitals xz, yz, and xy is due to an orbital-blocking mechanism, realized by large Hund's coupling leading to a singlet high-spin ground state which prohibits mixing of orbitals. The strength of this effect depends, in part, on the crystal geometry. There is a difference in the next nearest neighbor hopping probability for the Fe $3d_{xz/yz}$ and Fe $3d_{xy}$ electrons. The two channels for this hopping,

direct and via the chalcogenide atom, have different signs. The latter channel depends on the pnictogen/chalcogen height above the iron plane, which, on the average, is larger in the chalcogenides than in the pnictides. A large enough chalcogen height then leads to a similar size of the two contributions for the d_{xy} orbital, resulting in a vanishing probability for the nearest neighbor hopping. This kinetic frustration mechanism leads to an enhancement of the effective mass for the Fe $3d_{xy}$ electrons, resulting in a stronger renormalization.

We find our data in good agreement with DFT + DMFT calculations performed by Aichhorn *et al.*, where an orbital-dependent renormalization in the range of 2 to 5 was predicted [30]. We believe this effect is seen in all investigated samples of the $FeSe_xTe_{1-x}$ series with the difference being that in the previous studies the $3d_{xy}$ band is shifted upwards to form the largest Fermi surface sheet while in FeSe the $3d_{xy}$ is situated below the two $3d_{xz/yz}$ bands. Comparing to the calculations for FeTe and FeSe presented in [10], this leads to the conclusion that the band structure of the previously investigated compounds is rather representative for the FeTe band structure, while our study on FeSe agrees very well with the calculations for FeSe. At this point it is important to mention that the samples investigated in the mentioned publications were all from the Te-rich side of the phase diagram. In our study on FeSe we are able to provide the first to our knowledge data on a single-crystalline sample from the Se-rich side. Whether there is a continuous upward shift of the d_{xy} band with increasing Te content or whether the change is abrupt cannot be said without additional data from the Se-rich side of the phase diagram.

We also find our data to be in very good agreement with the recent work on thick films reported in [31]. We suggest that our data represent the bulk band structure of FeSe and are therefore suitable for comparison with monolayer samples to investigate the role of interface and surface effects leading to their largely enhanced critical temperature.

Recently we became aware of related work by Nakayama *et al.* [32]. Contrary to their results, as shown above we did not observe any features in the spectra which are not explained by the regular band structure calculations and therefore any signature of the nematic order in this material.

[1] Y. Kamihara, H. Hiramatsu, M. Hirano, R. Kawamura, H. Yanagi, T. Kamiya, and H. Hosono, J. Am. Chem. Soc. **128**, 10012 (2006).

[2] M. H. Fang, H. M. Pham, B. Qian, T. J. Liu, E. K. Vehstedt, Y. Liu, L. Spinu, and Z. Q. Mao, Phys. Rev. B **78**, 224503 (2008).

[3] R. Khasanov, M. Bendele, A. Amato, P. Babkevich, A. T. Boothroyd, A. Cervellino, K. Conder, S. N. Gvasaliya, H. Keller, H.-H. Klauss, H. Luetkens, V. Pomjakushin,

E. Pomjakushina, and B. Roessli, Phys. Rev. B **80**, 140511 (2009).

[4] K.-W. Yeh, T.-W. Huang, Y.-l. Huang, T.-K. Chen, F.-C. Hsu, P. M. Wu, Y.-C. Lee, Y.-Y. Chu, C.-L. Chen, J.-Y. Luo, D.-C. Yan, and M.-K. Wu, Europhys. Lett. **84**, 37002 (2008).

[5] F.-C. Hsu, J.-Y. Luo, K.-W. Yeh, T.-K. Chen, T.-W. Huang, P. M. Wu, Y.-C. Lee, Y.-L. Huang, Y.-Y. Chu, D.-C. Yan, and M.-K. Wu, Proc. Natl. Acad. Sci. USA **105**, 14262 (2008).

[6] Q.-Y. Wang, Z. Li, W.-H. Zhang, Z.-C. Zhang, J.-S. Zhang, W. Li, H. Ding, Y.-B. Ou, P. Deng, K. Chang, J. Wen, C.-L. Song, K. He, J.-F. Jia, S.-H. Ji, Y.-Y. Wang, L.-L. Wang, X. Chen, X.-C. Ma, and Q.-K. Xue, Chinese Phys. Lett. **29**, 037402 (2012).

[7] S. He, J. He, W. Zhang, L. Zhao, D. Liu, X. Liu, D. Mou, Y.-B. Ou, Q.-Y. Wang, Z. Li, L. Wang, Y. Peng, Y. Liu, C. Chen, L. Yu, G. Liu, X. Dong, J. Zhang, C. Chen, Z. Xu, X. Chen, X. Ma, Q. Xue, and X. J. Zhou, Nat. Mater. **12**, 605 (2013).

[8] F. Chen, B. Zhou, Y. Zhang, J. Wei, H.-W. Ou, J.-F. Zhao, C. He, Q.-Q. Ge, M. Arita, K. Shimada, H. Namatame, M. Taniguchi, Z.-Y. Lu, J. Hu, X.-Y. Cui, and D. L. Feng, Phys. Rev. B **81**, 014526 (2010).

[9] Y. Lubashevsky, E. Lahoud, K. Chashka, D. Podolsky, and A. Kanigel, Nat. Phys. **8**, 309 (2012).

[10] A. Tamai, A. Y. Ganin, E. Rozbicki, J. Bacsa, W. Meevasana, P. D. C. King, M. Caffio, R. Schaub, S. Margadonna, K. Prassides, M. J. Rosseinsky, and F. Baumberger, Phys. Rev. Lett. **104**, 097002 (2010).

[11] H. Miao, P. Richard, Y. Tanaka, K. Nakayama, T. Qian, K. Umezawa, T. Sato, Y.-M. Xu, Y. B. Shi, N. Xu, X.-P. Wang, P. Zhang, H.-B. Yang, Z.-J. Xu, J. S. Wen, G.-D. Gu, X. Dai, J.-P. Hu, T. Takahashi, and H. Ding, Phys. Rev. B **85**, 094506 (2012).

[12] K. Nakayama, T. Sato, P. Richard, T. Kawahara, Y. Sekiba, T. Qian, G. F. Chen, J. L. Luo, N. L. Wang, H. Ding, and T. Takahashi, Phys. Rev. Lett. **105**, 197001 (2010).

[13] D. Liu, W. Zhang, D. Mou, J. He, Y.-B. Ou, Q.-Y. Wang, Z. Li, L. Wang, L. Zhao, S. He, Y. Peng, X. Liu, C. Chen, L. Yu, G. Liu, X. Dong, J. Zhang, C. Chen, Z. Xu, J. Hu, X. Chen, X. Ma, Q. Xue, and X. J. Zhou, Nat. Commun. **3**, 931 (2012).

[14] J.-Y. Lin, Y. S. Hsieh, D. A. Chareev, A. N. Vasiliev, Y. Parsons, and H. D. Yang, Phys. Rev. B **84**, 220507 (2011).

[15] D. Chareev, E. Osadchii, T. Kuzmicheva, J.-Y. Lin, S. Kuzmichev, O. Volkova, and A. Vasiliev, CrystEngComm **15**, 1989 (2013).

[16] A. E. Böhmer, F. Hardy, F. Eilers, D. Ernst, P. Adelmann, P. Schweiss, T. Wolf, and C. Meingast, Phys. Rev. B **87**, 180505 (2013).

[17] T. M. McQueen, Q. Huang, V. Ksenofontov, C. Felser, Q. Xu, H. Zandbergen, Y. S. Hor, J. Allred, A. J. Williams, D. Qu, J. Checkelsky, N. P. Ong, and R. J. Cava, Phys. Rev. B **79**, 014522 (2009).

[18] T. Miyake, K. Nakamura, R. Arita, and M. Imada, J. Phys. Soc. Japan **79**, 044705 (2010).

[19] A. Subedi, L. Zhang, D. J. Singh, and M. H. Du, Phys. Rev. B **78**, 134514 (2008).

[20] Y. Xia, D. Qian, L. Wray, D. Hsieh, G. F. Chen, J. L. Luo, N. L. Wang, and M. Z. Hasan, Phys. Rev. Lett. **103**, 037002 (2009).

[21] T. Yoshida, S.-I. Ideta, I. Nishi, A. Fujimori, M. Yi, R. G. Moore, S.-K. Mo, D. Lu, Z.-X. Shen, Z. Hussain, K. Kihou, P. M. Shirage, H. Kito, C.-H. Lee, A. Iyo, H. Eisaki, and H. Harima, Front. Phys. **2**, 1 (2014).

[22] G. Lee, H. S. Ji, Y. Kim, C. Kim, K. Haule, G. Kotliar, B. Lee, S. Khim, K. H. Kim, K. S. Kim, K.-S. Kim, and J. H. Shim, Phys. Rev. Lett. **109**, 177001 (2012).

[23] A. I. Coldea, J. D. Fletcher, A. Carrington, J. G. Analytis, A. F. Bangura, J.-H. Chu, A. Erickson, I. Fisher, N. E. Hussey, and R. D. McDonald, Phys. Rev. Lett. **101**, 216402 (2008).

[24] L. de' Medici, S. R. Hassan, M. Capone, and X. Dai, Phys. Rev. Lett. **102**, 126401 (2009).

[25] R. Yu and Q. Si, Phys. Rev. B **84**, 235115 (2011).

[26] J. Maletz, V. B. Zabolotnyy, D. V. Evtushinsky, A. N. Yaresko, A. A. Kordyuk, Z. Shermadini, H. Luetkens, K. Sedlak, R. Khasanov, A. Amato, A. Krzton-Maziopa, K. Conder, E. Pomjakushina, H.-H. Klauss, E. D. L. Rienks, B. Büchner, and S. V. Borisenko, Phys. Rev. B **88**, 134501 (2013).

[27] C.-L. Song, Y.-L. Wang, P. Cheng, Y.-P. Jiang, W. Li, T. Zhang, Z. Li, K. He, L. Wang, J.-F. Jia, H.-H. Hung, C. Wu, X. Ma, X. Chen, and Q.-K. Xue, Science **332**, 1410 (2011).

[28] For the spectral function, the following model was used: $A(\boldsymbol{k},\omega) = 2\pi [u_{\boldsymbol{k}}^2 \delta(\omega - E_{\boldsymbol{k}}) + v_{\boldsymbol{k}}^2 \delta(\omega + E_{\boldsymbol{k}})]$ with $u_{\boldsymbol{k}}^2 = \frac{1}{2}(1 + \frac{\epsilon_{\boldsymbol{k}}}{E_{\boldsymbol{k}}}), v_{\boldsymbol{k}}^2 = \frac{1}{2}(1 - \frac{\epsilon_{\boldsymbol{k}}}{E_{\boldsymbol{k}}}), E_{\boldsymbol{k}} = \sqrt{\epsilon_{\boldsymbol{k}}^2 + \Delta^2}$. For further explanations see D. V. Evtushinsky, T. K. Kim, A. A. Kordyuk, V. B. Zabolotnyy, B. Buechner, A. V. Boris, D. L. Sun, C. T. Lin, H. Q. Luo, Z. S. Wang, H. H. Wen, R. Follath, and S. V. Borisenko, arXiv:1106.4584.

[29] Z. P. Yin, K. Haule, and G. Kotliar, Nat. Mater. **10**, 932 (2011).

[30] M. Aichhorn, S. Biermann, T. Miyake, A. Georges, and M. Imada, Phys. Rev. B **82**, 064504 (2010).

[31] S. Tan, Y. Zhang, M. Xia, Z. Ye, F. Chen, X. Xie, R. Peng, D. Xu, Q. Fan, H. Xu, J. Jiang, T. Zhang, X. Lai, T. Xiang, J. Hu, B. Xie, and D. Feng, Nat. Mater. **12**, 634 (2013).

[32] K. Nakayama, Y. Miyata, G. N. Phan, T. Sato, Y. Tanabe, T. Urata, K. Tanigaki, and T. Takahashi, arXiv:1404.0857.

[33] See Supplemental Material at http://link.aps.org/supplemental/10.1103/PhysRevB.89.220506 for additional energy-momentum cuts at different excitation energies, additional Fermi surface maps, wide-angle- and wide-energy-window spectra of the Brillouin zone center, and symmetry considerations regarding the experiment.